ADVANCED FUNCTIONAL MATERIALS
www.afm-journal.de

Non-Covalent Molecular Engineering of Hydrogel Electrolytes via π-Anion Confinement and Hydrogen-Bond Reconfiguration for Wide-Temperature and Ultra-Stable Zn-Ion Batteries

Jia Zhong, Chuqiao Xia, Tianyu Zhang, Hongfei Wang, Haolan Tao,* Cheng Lian, and Yong Hu**

The practical application of Zn-ion batteries (ZIBs) is hindered by poor cycling stability and a narrow operating temperature window, issues stemming from the unstable Zn anode and the reactive nature of aqueous electrolyte. To overcome these challenges, a functional hydrogel electrolyte is developed via copolymerization of acrylamide (AM) and 2-phenoxyethyl acrylate (PHEA). This design utilizes a novel non-covalent molecular engineering strategy to simultaneously regulate Zn^{2+} transport and enhance thermal adaptability. Specifically, the electron-deficient phenyl rings in PHEA establish favorable π-anion interactions with OTf^- anions, achieving a high Zn^{2+} transference number of 0.70. Concurrently, spectroscopic analyses indicate that the oxygen-rich groups in PHEA act as competitive hydrogen-bond acceptors, reconstructing the hydrogel's hydrogen-bonding network. This reconfiguration leads to tighter confinement of water molecules and a broader operational temperature range. Consequently, Zn//Zn symmetric cells demonstrate exceptional cycling durability over 6400 h at 25 °C, 2400 h at 50 °C, and 1200 h at –20 °C. When paired with $Zn_2V_2O_7$ cathodes, full cells also deliver outstanding cycling performance and remarkable capacity retention across this wide temperature range. This work provides fundamental insights into non-covalent interactions for electrolyte design and presents a scalable strategy for developing robust, temperature-resilient energy storage.

1. Introduction

The rapid expansion of flexible and wearable electronics, such as health and motion monitors, creates strong demand for safe, durable, and stretchable rechargeable batteries. Aqueous zinc-ion batteries (ZIBs) have emerged as a promising candidate due to their high theoretical capacity (820 mAh g^{-1}), inherent safety, high ionic conductivity, and low cost.[1,2] However, the practical application of ZIBs is hindered by persistent issues at the Zn metal anode, including dendrite formation, corrosion, and hydrogen evolution reactions (HER).[3,4] These problems originate from the strong solvation of Zn^{2+} ions, the reactivity of water molecules, and uneven ion flux.[5–7] The strong cation-anion coupling in conventional aqueous electrolytes further reduces the Zn^{2+} transference number and Coulombic efficiency (CE), limiting anode reversibility.[3,8] These challenges are exacerbated under extreme temperatures, where unstable ion transport and variable water activity lead to rapid performance degradation.[1] Therefore, developing advanced electrolyte designs that enable highly reversible Zn plating/stripping across a wide temperature range is critically important.[9,10]

Hydrogel electrolytes containing zincophilic functional groups, such as sodium polyacrylate (PANa), poly(vinyl alcohol) (PVA), and polyacrylamide (PAM), could facilitate 3D diffusion of Zn^{2+} ions and help regulate ionic transport pathways.[11,12] Among various polymer matrices,

J. Zhong, C. Xia, H. Wang
Key Laboratory of the Ministry of Education for Advanced Catalysis Materials
Department of Chemistry
Zhejiang Normal University
Jinhua 321004, P. R. China
E-mail: whf0614@zjnu.edu.cn

T. Zhang, Y. Hu
Institute of Nanocatalysis and Energy Conversion
College of Chemistry and Materials Engineering
Zhejiang A&F University
Hangzhou 311300, P. R. China
E-mail: yonghu@zafu.edu.cn

H. Tao, C. Lian
State Key Laboratory of Chemical Engineering
School of Chemistry and Molecular Engineering
East China University of Science and Technology
Shanghai 200237, P. R. China
E-mail: haolan_tao@ecust.edu.cn

The ORCID identification number(s) for the author(s) of this article can be found under https://doi.org/10.1002/adfm.202527894

DOI: 10.1002/adfm.202527894

PAM-based hydrogel electrolytes are particularly promising due to their straightforward synthesis and comparatively low cost.[13] Nevertheless, current PAM hydrogel electrolytes still face several critical challenges, such as limited ion transport efficiency, high water evaporation rates, and inadequate mechanical strength.[14,15] Furthermore, existing PAM hydrogels remain ineffective in resolving the fundamental issues associated with Zn anodes.[16] These persistent problems are largely attributed to unresolved difficulties within the electrolyte bulk and at the electrode/electrolyte interface.[17–19]

Recently, copolymerization with functional molecules has emerged as one of the most effective approaches for enhancing both the physicochemical and electrochemical properties of PAM hydrogels.[18] By incorporating tailored groups into the polymer network, this method considerably improves mechanical strength, ionic conductivity, and interfacial compatibility.[20,21] Despite these benefits, several important limitations have yet to be resolved. The current approach still falls short in effectively suppressing anion migration, which contributes to significant concentration polarization. Furthermore, existing functional copolymerization methods have not adequately enhanced the adaptability of Zn^{2+} transport and deposition behavior across a broad range of temperatures.[21–23]

Noncovalent interactions play a crucial role in impact-resistant polymer materials by acting as sacrificial bonds that efficiently dissipate mechanical energy, thereby endowing the materials with superior functionalities.[24] Hydrogen bonding, as a classic example, has been widely employed in hydrogel networks to effectively regulate the activity and behavior of water molecules.[25] Through strategic manipulation of such bonding, it becomes possible to regulate freezing and evaporation processes within the electrolyte, thereby effectively broadening its operational temperature range.[26] This approach provides a promising pathway for developing advanced energy storage systems capable of functioning reliably under extreme environmental conditions.[27] In contrast to conventional noncovalent interactions (hydrogen bonds, hydrophobic interactions, and ion pairs), π-ion interactions represent a distinct class of electrostatic attractions between ions and π-electron systems.[28] These interactions are increasingly recognized as significant noncovalent forces that play a crucial role in modulating the structure and function of various molecular assemblies. Li et al. demonstrated that introducing ninhydrin molecules as additives into a $ZnSO_4$ electrolyte enables the electron-deficient aromatic rings to anchor SO_4^{2-} ions via π-anion interactions. This dynamic and balanced ion-enriched interface effectively suppresses Zn dendrite growth induced by the space charge layer.[29] Constructing aromatic structures in hydrogel networks to leverage π-ion interactions is a viable, yet unreported, strategy for tuning ion transport from the bulk electrolyte to the electrode interface. Therefore, copolymerizing acrylamide (AM) with specially designed monomers to harness noncovalent interactions among the polymer network, ions, and water molecules presents a highly feasible approach for enhancing the functional performance of hydrogel electrolytes.

In this work, we propose a strategy of copolymerizing AM monomers with 2-phenoxyethyl acrylate (PHEA) in the presence of $Zn(OTf)_2$ to fabricate a functional poly(AM-co-PHEA) (PAP) hydrogel electrolyte. This design orchestrates intrinsic non-covalent interactions to stabilize the electrolyte/Zn-metal interface. The electron-deficient aromatic motifs in PHEA promote π-anion interactions, thereby reducing anion mobility. Concurrently, the abundant ether-ester linkages disrupt the native hydrogen-bonding network of water. This suppression of water activity effectively inhibits the HER and enhances battery performance over a wide temperature range. Consequently, Zn^{2+} ions can migrate rapidly along the extended polymer chains, achieving a high transference number of 0.70 and leading to uniform deposition. Thanks to these outstanding characteristics, the PAP hydrogel electrolyte enables ultra-long cycling stability exceeding 6400 h in Zn//Zn symmetric cells at room temperature. It also maintains stable operation for over 2400 h at 50 °C and 1200 h at −20 °C. These improved electrochemical characteristics are also demonstrated in $Zn//Zn_2V_2O_7$ (ZVO) full batteries, which exhibit exceptional cycling stability across a broad temperature range. By offering a fundamental molecular-level insight, this work advances the design of hydrogel electrolytes toward highly durable and temperature-adaptive Zn-based energy storage.

2. Results and Discussion

As a key component of flexible energy storage devices, hydrogel electrolytes should simultaneously meet several critical requirements, such as high ion transport kinetics, robust mechanical stability, consistent electrode/electrolyte interfacial chemistry, and broad environmental adaptability.[30] To address this, we implemented a molecular engineering approach by copolymerizing AM with PHEA, a polymer incorporating benzene rings and oxygen-rich functional groups (ester and ether bonds), to fabricate the PAP hydrogel electrolyte (**Figure 1a**). For comparative purposes, a PAM-based hydrogel electrolyte was also synthesized as a control sample. In addition to the covalent interactions commonly present in the PAP polymer network, the incorporation of PHEA leverages its intrinsic molecular structure to modulate the electrochemical behavior of ions and water molecules through a series of non-covalent interactions. The introduction of oxygen-rich functional groups (ester and ether groups) enhances the hydrogen-bond donating capacity, thereby more effectively restricting the activity of water molecules.[31,32] More significantly, the aromatic units in PHEA, which possess an electron-withdrawing property, can engage with OTf^- anions to form special π-anion interactions. This facilitates the dissociation of Zn^{2+} and OTf^- ions.[29,32] As a result, Zn^{2+} migration pathways can be established along the flexible polymer chains, which not only facilitates Zn^{2+} transport but also enhances the stability of electrochemical reactions at the anode/electrolyte interface.

The chemical structure of the synthesized hydrogels was verified using attenuated total reflection Fourier transform infrared (ATR-FTIR) spectroscopy, as shown in Figure 1b. The absorption band observed from 1403 to 1602 cm^{-1} corresponds to the C–C vibrational mode of the benzene ring skeleton. Besides, peaks identified at 949 and 1729 cm^{-1} are associated with the stretching vibrations of C–O–C and O–C=O bonds, respectively.[33–35] Correspondingly, the detection of characteristic functional groups from both PHEA and AM in the spectra confirms the successful formation of the PAP hydrogel. The morphology of the PAP hydrogel was analyzed by scanning electron microscopy (SEM), revealing a hierarchically ordered porous structure similar to that of PAM, but with an increased average pore size of 10.3 μm

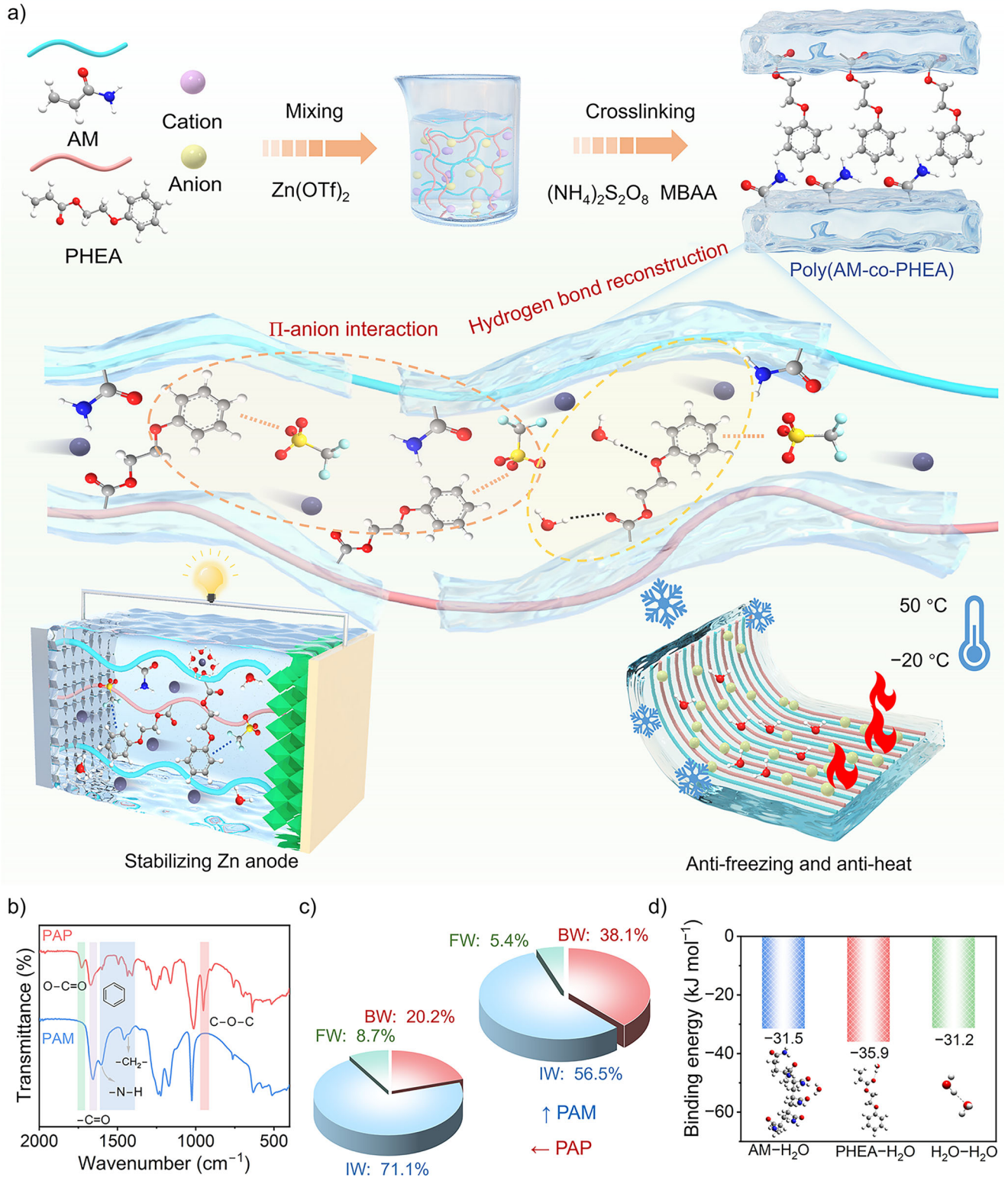

Figure 1. Preparation and characterization of the PAP hydrogel. a) Schematic illustration for the synthesis of PAP. b) ATR-FTIR of PAP and PAM. c) Quantitative distribution of water molecules in various states, as determined from Raman spectra. d) Binding energies of water molecules with various components.

compared to 6.6 µm for the latter (Figure S1, Supporting Information). This distinctive porous framework is expected to facilitate Zn^{2+} migration and promote a uniform electric field distribution across the anode interface. The mechanical properties of hydrogel electrolytes play a critical role in determining the ability of ZIBs to withstand external mechanical deformation. Corresponding deformation tests confirm the practical robustness of the PAP hydrogel. As shown in Figure S2 (Supporting Information), the hydrogel withstands significant stretching and twisting without damage, demonstrating excellent mechanical resilience. Tensile testing results indicate that the PAP hydrogel exhibits significantly enhanced mechanical performance (Figure S3a, Supporting Information), with a tensile stress of 130.0 kPa and a tensile strain of 115.8%, both of which are substantially higher than those of the PAM hydrogel (20.3 kPa and 46.4%). Moreover, the PAP hydrogel demonstrates an elastic modulus of 98.1 kPa and a toughness of 88.2 kJ m^{-3}, as presented in Figure S3b (Supporting Information), values that also exceed those of the PAM hydrogel (66.2 kPa and 7.1 kJ m^{-3}). The enhanced strength and toughness of the hydrogel originate from the amphiphilic nature of PHEA. Its hydrophilic oxygen-rich groups contribute to water retention, whereas the hydrophobic aromatic regions induce microphase separation, thereby improving mechanical stability.[36]

To gain a comprehensive understanding of the physicochemical properties of the PAP hydrogel electrolyte, Raman spectroscopy was employed to analyze the interactions between polymer chains and water molecules. The broad O–H stretching bands can be classified into three distinct water states using Gaussian fitting: 1) "bond water" (BW) at 3235 cm^{-1}, corresponding to water molecules with strong hydrogen bonding and a coordination number close to 4; 2) "intermediate water" (IW) at 3452 cm^{-1}, which features distorted hydrogen bonds and incomplete connectivity to surrounding water molecules; and 3) "free water" (FW) at 3622 cm^{-1}, representing unbound water molecules in the form of monomers, dimers, or trimers that exhibit minimal interaction with their environment (Figure S4, Supporting Information).[37,38] The proportion of BW in the PAP hydrogel decreases, whereas that of IW and FW increases (Figure 1c), suggesting that PHEA facilitates the transformation of BW into IW and FW. This observation indicates a partial breakdown of the original hydrogen-bonding network among water molecules, accompanied by a significant enhancement in polymer-water interactions.[39] Such a change contributes to the suppression of the HER and improves tolerance to external temperature variations. Moreover, ^{2}H nuclear magnetic resonance (NMR) spectroscopy reveals an upfield shift in the water proton signals, suggesting increased electron density and restricted mobility of water molecules resulting from hydrogen bonding with polar groups in the polymer matrix.[39,40] As illustrated in Figure S5 (Supporting Information), the PAP hydrogel displays a more distinct upfield shift compared to PAM, providing further evidence of its superior water confinement ability. Owing to this effective immobilization of water molecules, the PAP hydrogel demonstrates notable thermal adaptability. Differential scanning calorimetry (DSC) results indicate a distinct exothermic peak near –18 °C in the pristine PAM hydrogel, which is associated with water crystallization (Figure S6, Supporting Information). In comparison, no such crystallization peaks are detected in the PAP hydrogel, confirming its significantly improved freeze tolerance due to the incorporation of PHEA chain segments.[41] Water retention tests directly confirm that the PAP hydrogel retains 55% of its initial water content after 96 h under ambient conditions, demonstrating significantly greater retention capability compared to the PAM hydrogel, which maintains only 32% (Figure S7, Supporting Information). The hydration behavior of the hydrogels was quantitatively evaluated using density functional theory (DFT) calculations, as presented in Figure 1d. The binding energy for the PHEA-H_2O system is calculated to be –35.9 kJ mol^{-1}, which is stronger than that of the AM-H_2O system (–31.5 kJ mol^{-1}) and the H_2O-H_2O dimer (–31.2 kJ mol^{-1}). This stronger interaction suggests further suppression of water molecule activity within the hydrogel, which is expected to promote the desolvation and migration of hydrated Zn^{2+} ions while concurrently suppressing the HER. On a molecular level, the incorporated PHEA chains abundant in oxygen-containing functional groups serve as competitive hydrogen-bond acceptors, effectively disrupting the self-associative network of water molecules. By sequestering water reactants within the polymer matrix, the hydrogel raises the energy barrier for the HER, thereby kinetically inhibiting its progression and shifting its thermodynamic potential to more negative values. Furthermore, the water molecules confined in this system exist in an energetically stabilized, "polymer-locked" state, which confers remarkable resilience against thermal fluctuations. Collectively, the mechanism that suppresses the HER also endows the material with operational stability across a wide temperature range, from below ambient to elevated conditions. This significantly broadens the device's operational window and highlights the promise of the PAP hydrogel as a high-performance electrolyte material for advanced battery systems.

To elucidate the intrinsic transport properties of Zn^{2+} ions within the PAP hydrogel, it is essential to understand the role of PHEA. The ionic conductivity and Zn^{2+} transference number of the hydrogel electrolytes were evaluated using electrochemical impedance spectroscopy (EIS). At 25 °C, the PAP hydrogel exhibits an ionic conductivity of 25.4 mS cm^{-1} (Figure S8, Supporting Information), surpassing that of the PAM hydrogel (18.3 mS cm^{-1}). This enhancement is attributed to the facilitated ion transport within the migration channels modified by PHEA. Furthermore, PAP maintains high ionic conductivities of 39.5 and 13.5 mS cm^{-1} as the temperature is adjusted to 50 and –20 °C, respectively. These values are in sharp contrast to the PAM hydrogel with 30.2 and 8.1 mS cm^{-1} at 50 and –20 °C, respectively, which reflects the superior extreme-temperature tolerance of PAP. Moreover, the PAP hydrogel electrolyte demonstrates a significantly higher Zn^{2+} transference number of 0.70 relative to the PAM-based electrolyte (0.47), as depicted in **Figures** 2a and S9 (Supporting Information). This enhancement in ion transport performance signifies improved charge transfer efficiency and restricted anion mobility in the PAP system, offering a potential pathway toward minimizing anion-related side reactions in Zn-based devices. X-ray photoelectron spectroscopy (XPS) and ^{1}H NMR spectroscopy were utilized to further examine the interaction between PHEA and OTf^{-}. Comparative XPS analysis was conducted on PAM and PAP samples (Figure S10, Supporting Information). Introduction of $Zn(OTf)_2$ into the PAP hydrogel network results in a positive shift in the F 1s peak relative to PAM, indicating a strong associative interaction between

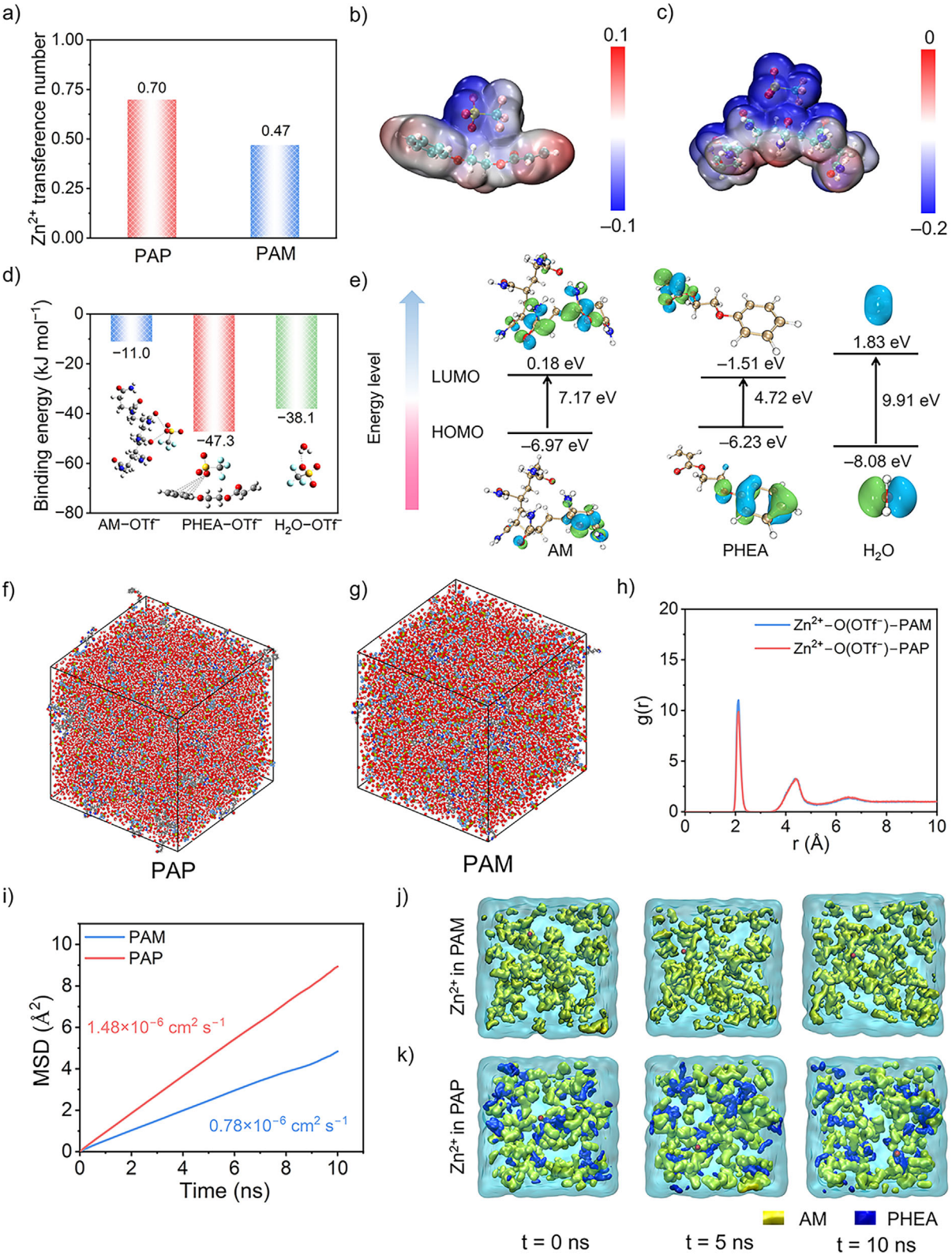

Figure 2. a) Comparison of Zn^{2+} transference number. ESP distribution of the b) OTf^--PHEA and c) OTf^--AM structures. d) Binding energies of OTf^- anions with various components. e) Calculated frontier molecular orbital energies of AM, PHEA, and H_2O molecules. 3D snapshots of MD simulations for f) PAP and g) PAM. h) Radial distribution functions for Zn^{2+}-O (OTf^- anions) collected in PAP and PAM. i) The function of MSDs vs time in PAP and PAM. Zn^{2+} diffusion pathways within j) PAM and k) PAP hydrogel matrices.

OTf^- anions and PHEA. Furthermore, ^1H NMR analysis reveals that upon incorporation of $Zn(OTf)_2$ into the PAP hydrogel network, the aromatic proton signals undergo substantial chemical shifts, providing firm evidence for the presence of π-anion interactions (Figure S11, Supporting Information).[42,43] The electrostatic potential (ESP) surface shows a complementary charge distribution between PAP and OTf^-, with the electron-deficient benzene ring and the electron-rich sulfonate group oriented in a spatially favorable arrangement for π-anion interaction, as illustrated in Figures 2b,c and S12 (Supporting Information).[42] Additionally, the binding energy between OTf^- and PHEA was calculated to be –47.3 kJ mol^{-1}, which is higher than that of OTf^- with AM (–11.0 kJ mol^{-1}) (Figure 2d). This result provides quantitative evidence supporting the ability of OTf^- to bind with benzene ring groups. In addition, the molecular orbital energy levels were calculated to evaluate the electron-accepting capabilities of all components (Figure 2e). The lowest unoccupied molecular orbital (LUMO) energy of PHEA is found to be significantly lower than those of AM and H_2O (–1.51 vs 0.18 and 1.83 eV, respectively), which also suggests that electrons from OTf^- anions are more likely to be transferred to the PHEA segment. Together, the data establish PHEA as a promising π-anion interaction acceptor, which facilitates efficient Zn^{2+} transport within the PAP hydrogel network.

Molecular dynamics (MD) simulations were employed to further investigate the coordination environment of Zn^{2+} ions within different hydrogel matrices. The simulations demonstrate notable differences in the regulatory influence of the polymer matrix on the Zn^{2+}-OTf^- interaction and the ionic transport kinetics, as depicted in Figure 2f,g. The radial distribution function (RDF) around Zn^{2+} ions shows that the formation of OTf^--benzene ring interactions in PHEA leads to a decreased number of OTf^- anions within the Zn^{2+} solvation shell in the PAP hydrogel system (Figure 2h). The diffusion dynamics of Zn^{2+} ions were also evaluated by calculating the mean square displacement (MSD) at room temperature (Figure 2i). Results indicate that the Zn^{2+} diffusion coefficient in PAP (1.48×10^{-6} cm^2 s^{-1}) is higher than that in PAM (0.78×10^{-6} m^2 s^{-1}), suggesting enhanced Zn^{2+} mobility. This acceleration can be attributed to the formation of efficient cation transport channels, facilitated by the anion-confining capability of electron-withdrawing benzene ring groups within the PHEA molecular chains.[44] Moreover, MD simulations offer detailed visualization of Zn^{2+} migration pathways within the hydrogel networks. Consistent with the MSD results, trajectory analysis indicates that the inclusion of PHEA in PAP establishes well-defined ion conduction channels, in contrast to the disordered diffusion pathways observed in PAM (Figure 2j,k). Therefore, this optimized network architecture considerably improves Zn^{2+} transport kinetics, owing to favorable coordination environments and reduced anion-induced retardation.[45]

Given the improved physicochemical properties of the hydrogel electrolyte, the long-term cycling stability of Zn electrodes during repeated plating/stripping was further examined by assessing electrochemical performances in both Zn//Cu and Zn//Zn cell configurations. As shown in **Figure 3a**, the Zn//Cu cell with the PAP hydrogel electrolyte demonstrates outstanding cycling performance, retaining an average CE of 98.9% over 1300 cycles at 1 mA cm^{-2}/1 mAh cm^{-2}. In contrast, the Zn/PAM/Cu cell degrades rapidly and fails within 650 cycles under identical conditions. Moreover, the Zn//Cu half-cell utilizing the PAP hydrogel electrolyte displays negligible variation in its voltage-capacity profiles over extended cycling, in sharp contrast to the pronounced voltage drift and progressive instability observed in the control cell (Figure 3b,c). This comparison underscores the exceptional interfacial stability and sustained cycling endurance afforded by the PAP-based hydrogel electrolyte.

Moreover, to evaluate the advantages of the non-covalently modulated hydrogel electrolyte, the electrochemical stability of Zn metal anodes was investigated using symmetric Zn//Zn cells. Under 1 mA cm^{-2}/1 mAh cm^{-2}, the cell with PAM hydrogel fails after 1700 h, likely due to voltage fluctuations caused by dendrite formation. In contrast, the cell incorporating the PAP electrolyte demonstrates significantly enhanced stability, operating consistently for over 6400 h with minimal polarization (Figure 3d). Even under harsh cycling conditions of 5 mA cm^{-2} and 5 mAh cm^{-2}, the cell using the PAP hydrogel electrolyte exhibits substantially improved cycling performance, achieving a service life of ≈560 h, which is considerably longer than 50 h obtained with the PAM-based hydrogel electrolyte (Figure S13, Supporting Information). Also, the Zn/PAP/Zn cell delivers outstanding resilience to variations in current density, sustaining consistent overpotentials across a broad spectrum from 1 to 20 mA cm^{-2} (Figure 3e). Notably, upon returning to 1 mA cm^{-2}, the cell exhibits a slightly lower polarization voltage than its initial value, indicating enhanced interfacial kinetics following high-rate cycling. In comparison, the PAM-based cell suffers from substantial voltage instability at 5 mA cm^{-2} before eventual failure. The improved cycling endurance arises from the PAP hydrogel's unique capability to facilitate Zn deposition kinetics via π-anion interactions that restrict OTf^- mobility, while consistently upholding interfacial stability across numerous cycles.[29] To further evaluate practical applicability, shelving-recovery tests were performed on Zn//Zn symmetric cells at 1 mA cm^{-2} and 1 mAh cm^{-2}, with a 20-h rest period after every 10 cycles (Figure S14, Supporting Information). The cell utilizing the PAP hydrogel electrolyte maintained stable operation for over 2000 h. In contrast, the cell with PAM failed within 900 h. This stark contrast in cycling longevity underscores the superior effectiveness of PAP in suppressing Zn dendrites and parasitic side reactions, confirming its high practical potential for durable ZIBs.

To validate the temperature adaptability of the PAP hydrogel electrolyte, its operational performance was systematically evaluated over a wide temperature range under extreme conditions. As depicted in Figure 3f,g, Zn//Zn symmetric cells remain stable for 2400 h at 50 °C and 1200 h at –20 °C. This exceptional thermal resilience is attributed to the designed water-confined networks within the PAP matrix, which inhibit freezing at subzero temperatures and reduce water reactivity at high temperatures, thus supporting consistent Zn electrochemistry over a wide operational span from –20 to 50 °C.[46] To further substantiate the exceptional temperature adaptability of the PAP hydrogel, the cycling performance of Zn//Zn symmetric cells utilizing the liquid electrolyte was systematically evaluated under varying temperature conditions (Figure S15, Supporting Information). The liquid electrolyte cell could only operate for ≈100 h at 25 °C, with its operational time becoming negligible at 50 and –20 °C. This comparative analysis clearly demonstrates that

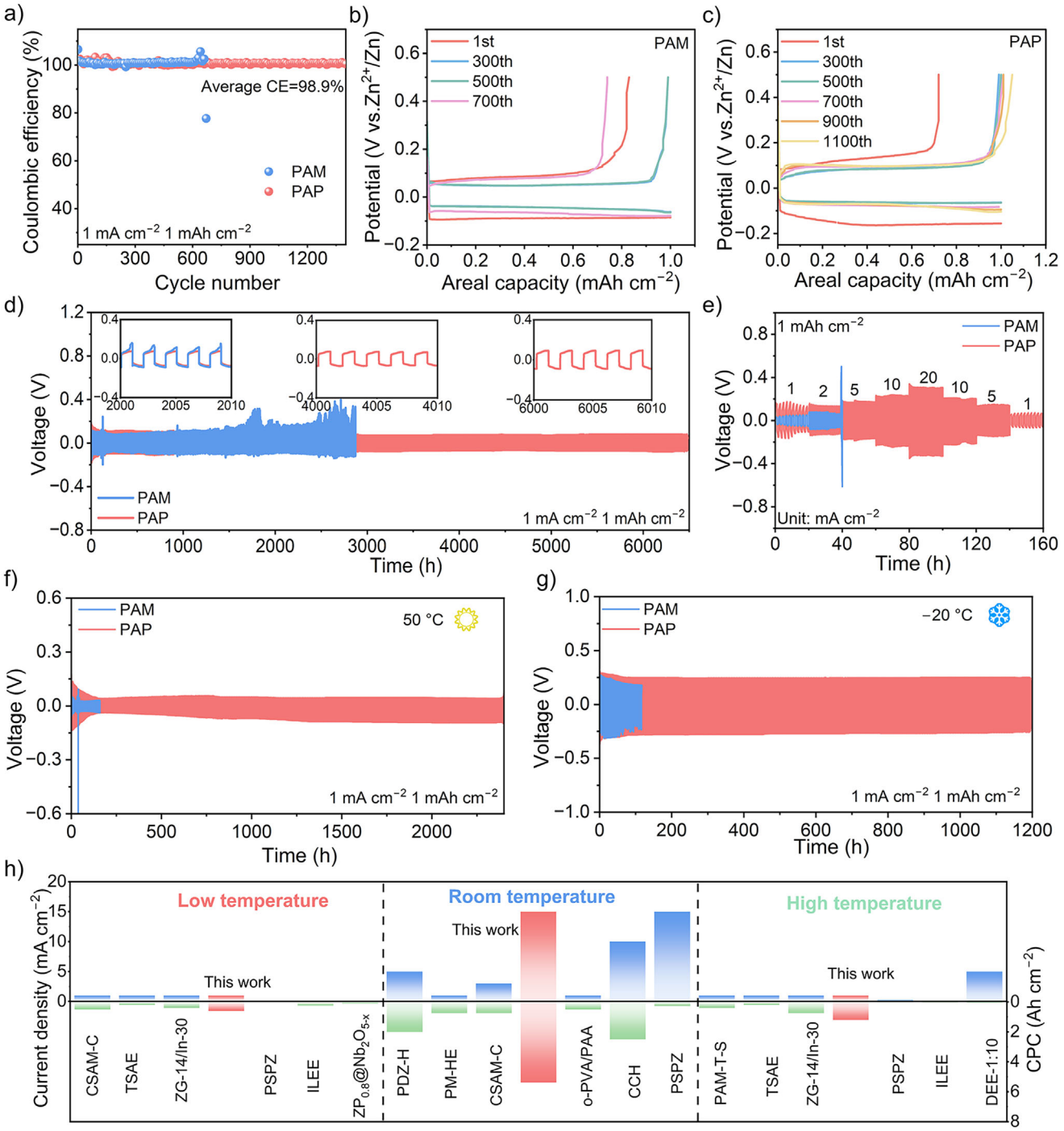

Figure 3. a) CE measurements and corresponding voltage-capacity profiles of b) Zn/PAM/Cu and c) Zn/PAP/Cu cells. d) Galvanostatic cycling of Zn//Zn cells with different hydrogel electrolytes at room temperature. e) Rate performance with a capacity of 1 mAh cm^{-2}. Cycling performances of Zn//Zn cells at f) 50 °C and g) −20 °C. h) Benchmarking of PAP against existing literature in current density and CPC across a wide temperature range.

the hydrogel electrolyte engineering strategy not only ensures cycling stability for reversible Zn plating/stripping but also confers significant environmental adaptability. The consistent electrochemical performance under thermal stress conditions confirms the material's ability to preserve interfacial integrity through optimized ion transport and interfacial chemistry. More impressively, comparative analysis with state-of-the-art hydrogel and non-hydrogel electrolytes confirms the superior performance of the PAP hydrogel, which achieves a substantially greater cumulative plating capacity (CPC) across both cryogenic and elevated temperature environments (Figure 3h; Tables S1–S3, Supporting Information).[47] These exceptional characteristics highlight the

potential of the PAP hydrogel as an advanced electrolyte material for next-generation Zn-based energy storage devices, combining outstanding environmental resilience with practical scalability suitable for extreme operational scenarios.

To further verify the stabilizing role of the PAP hydrogel electrolyte in Zn anode electrochemistry, a series of electrochemical and morphological analyses was carried out. Chronoamperometry (CA) was initially employed to investigate the influence of PAP on Zn deposition behavior (**Figure 4a**). In the PAM electrolyte, Zn deposition follows a typical 2D diffusion mechanism accompanied by a continuous rise in current density. This leads to nonuniform nucleation and accelerated dendritic growth, ultimately resulting in disordered and porous Zn structures. In contrast, the PAP hydrogel electrolyte promotes a stable 3D diffusion process, facilitated by rapid nucleation during the initial phase. This mechanism encourages dense and uniform Zn deposition with improved morphological integrity. EIS was performed on Zn//Zn cells at temperatures ranging from 40 to 80 °C to investigate Zn deposition behavior in different electrolytes (Figure S16, Supporting Information). The charge transfer resistance (R_{ct}) values of the cell with PAP electrolyte are consistently lower than those with PAM across all temperatures, indicating enhanced interfacial charge transfer kinetics. According to the Arrhenius equation, the activation energy (E_a) of PAP was calculated to be 34.9 kJ mol^{-1}, which is lower than that of PAM (37.7 kJ mol^{-1}). Since the desolvation process is typically the rate-limiting step in Zn electrochemical deposition, the reduced E_a suggests a lower desolvation energy barrier and improved Zn deposition/diffusion kinetics. This enhancement is attributed to the reconstructed hydrogen-bond network and restricted OTf^- anion mobility within the PAP electrolyte.[45]

To assess the suppression of side reactions, the electrochemical stability of various electrolytes was evaluated using linear sweep voltammetry (LSV) at a scan rate of 10 mV s^{-1} and linear polarization measurement, respectively. LSV measurements of Ti//Ti cells reveal that the PAP hydrogel possesses an electrochemical stability potential window (ESPW) of 2.75 V, broader than the 2.58 V of PAM (Figure S17, Supporting Information). The negligible current density observed confirms its excellent stability, affirming its suitability as a robust electrolyte. Besides, the PAP hydrogel electrolyte demonstrates a higher hydrogen evolution overpotential on the Zn foil surface than PAM at an identical current density (Figure 4b), indicating its enhanced ability to inhibit the HER. The superior HER suppression achieved by the PAP hydrogel electrolyte originates from a reengineered hydrogen bonding network that effectively modulates water reactivity. The decreased BW content, which is characterized by elevated thermodynamic activity and reduced reduction energy barriers, directly limits the population of reactive water molecules available for HER initiation at the Zn anode interface. Simultaneously, the increased proportions of IW and FW species maintain efficient ion transport while demonstrating markedly lower participation in parasitic reduction pathways. Consequently, this reconfigured hydrogen bonding environment synergistically elevates the HER activation barrier, minimizes gaseous byproduct formation, and promotes superior electrode/electrolyte interface stability. Tafel analysis (Figure 4c) further supports this result, revealing that PAP exhibits a lower corrosion current density (1.44×10^{-5} A cm^{-2}) and a higher corrosion potential (0.009 V), which collectively indicate enhanced corrosion resistance at the interface.[41] The influence of different electrolytes on the Zn deposition process was visualized in real-time using an in situ optical microscope at a current density of 10 mA cm^{-2}. In the case of the PAM hydrogel electrolyte, loose sediment begins to form within 10 min, followed by the development of pronounced Zn dendrites and a highly uneven surface after 30 min (Figure 4d). In contrast, the Zn anode in the PAP hydrogel electrolyte maintains a smooth, compact, and dendrite-free deposition layer after the same duration (Figure 4e), demonstrating its effective suppression of side reactions and regulation of uniform Zn nucleation. The surface morphology of Zn electrodes was examined using optical photography and SEM after 50 plating/stripping cycles at 1 mA cm^{-2} and 1 mAh cm^{-2}. In the PAM hydrogel electrolyte, Zn deposition exhibits a disordered and porous structure composed of flake-like dendritic formations (Figure 4f). Conversely, deposition in the PAP hydrogel electrolyte results in a densely packed and well-aligned arrangement of Zn deposits, yielding a smooth electrode surface (Figure 4g). The preferential exposure of the (002) crystal plane serves as an effective strategy for suppressing Zn dendrite growth, owing to its low surface energy and densely packed atomic arrangement.[48] The crystalline structures of cycled Zn electrodes in different electrolytes were characterized by the X-ray diffraction (XRD) technique (Figure S18, Supporting Information). The intensity ratio I_{002}/I_{101} for the PAP electrolyte (0.40) is higher than that for PAM (0.19), indicating that PAP promotes preferential Zn deposition along the (002) plane, thereby contributing to a highly stable Zn anode. As shown in Figure 4h,i, the morphology of deposited Zn was further examined using laser confocal scanning microscopy (CLSM). After cycling, the PAP-based electrode displays a notably smoother and more uniform surface, whereas the PAM-based sample exhibits significant fluctuations and prominent dendritic structures. The average surface roughness (S_a) of the deposit with the PAM hydrogel electrolyte reaches 10.8 µm, compared to only 3.8 µm for the PAP hydrogel electrolyte, reflecting the more homogeneous Zn deposition process enabled by PAP. The stability of electrochemical reactions at the Zn anode interface is closely linked to the suppression of water activity and restriction of free anion migration. The transport behavior of OTf^- anions near the electrode/electrolyte interface during electroplating was monitored using in situ Raman spectroscopy. Tracking the Raman signal ≈1035 cm^{-1} (associated with OTf^-) near the electrode reflects changes in anion concentration throughout the deposition process.[3] Notably, a distinct blueshift was observed in the OTf^- peak in PAP compared to that in PAM, indicating effective confinement of OTf^- anions by the PHEA network.[29] In the PAM electrolyte, the peak intensity decreases significantly after ≈20 min of plating (Figure 4j), suggesting an unstable interfacial mass transfer process and heightened concentration polarization. In contrast, the signal remains stable during the entire plating process with the PAP electrolyte (Figure 4k), demonstrating uniform ion distribution attributable to π-anion interactions.[49]

Based on the experimental and theoretical evidence presented above, a mechanistic model for Zn plating/stripping in different electrolyte systems is proposed. In the PAM electrolyte, Zn^{2+} ions undergo lateral diffusion across the electrode surface with uneven nucleation sites, preferentially depositing at energetically favorable locations, which leads to uncontrolled dendritic

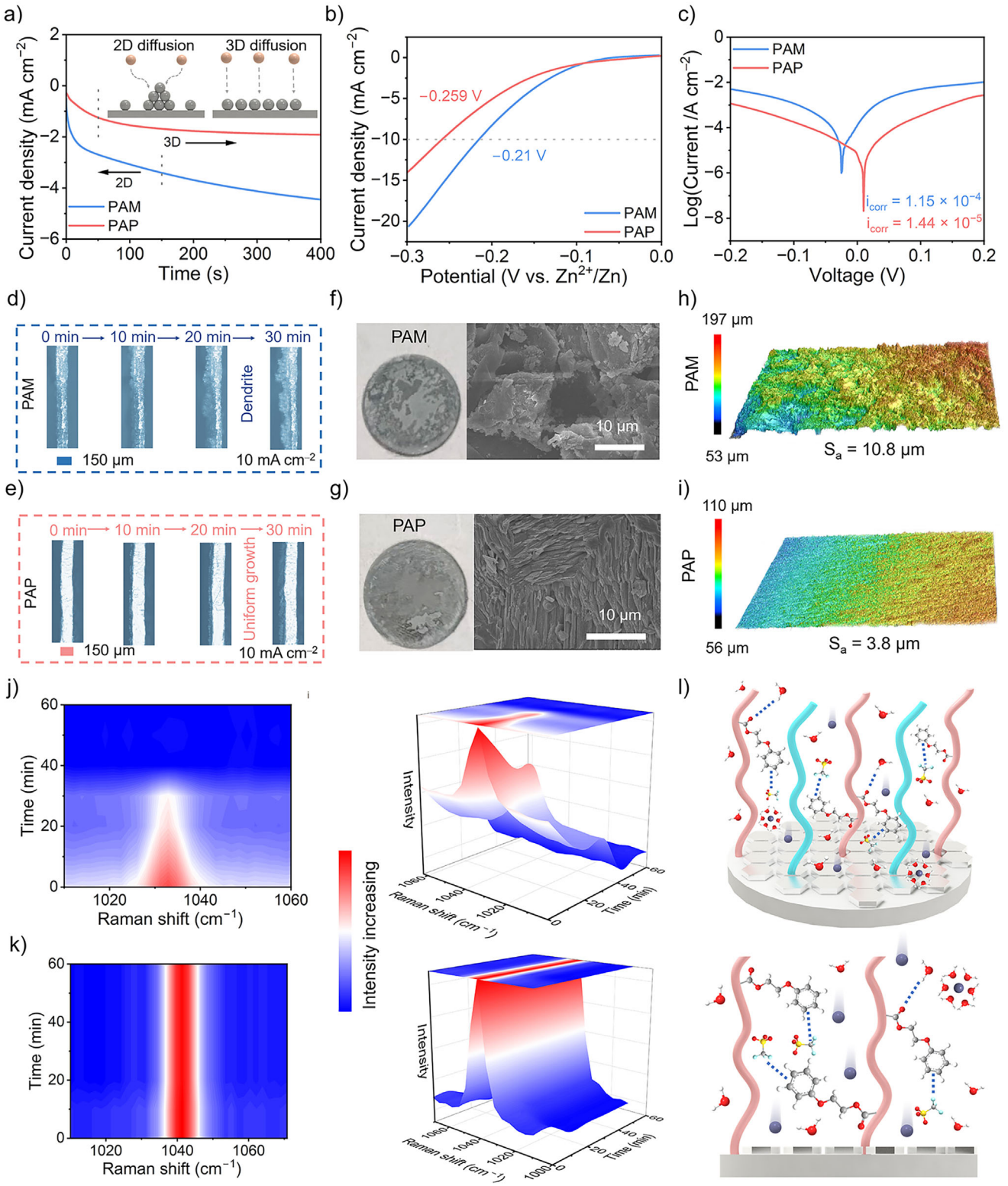

Figure 4. a) CA curves, b) LSV curves, and c) Tafel curves of Zn foils in different hydrogel electrolytes. In situ optical microscopy images of Zn//Zn cells using d) PAM and e) PAP hydrogel electrolytes. SEM images of Zn anodes after 50 cycles with f) PAM and g) PAP hydrogel electrolytes. CLSM images of Zn anodes after 50 cycles with h) PAM and i) PAP hydrogel electrolytes. In situ Raman spectra of Zn anodes were tested with j) PAM and k) PAP. l) Schematic diagram of Zn deposition in the PAP hydrogel electrolyte.

growth. In contrast, within the PAP electrolyte (Figure 4l), free water molecules are effectively confined within the hydrogel network through strong molecular interactions, thereby suppressing side reactions and enhancing tolerance to temperature variations. Furthermore, the electron-withdrawing aromatic groups in the PHEA framework preferentially attract OTf^- anions, which promotes rapid Zn^{2+} migration through the 3D porous matrix and facilitates uniform deposition on the Zn electrode surface. As a result, the PAP hydrogel electrolyte effectively inhibits Zn dendrite formation and reduces by-product accumulation, contributing to the achievement of a highly stable Zn electrode.

To evaluate the practical applicability of the PAP hydrogel electrolyte, full-cell batteries were constructed using Zn metal anodes coupled with ZVO cathodes.[50] As shown in the XRD pattern (Figure S19, Supporting Information), all major diffraction peaks of the cathode material match well with the standard phase of ZVO (JCPDS: 70-1532) and its characteristic C2/c space group symmetry. Furthermore, the SEM image confirms the successful synthesis of the ZVO cathode, which exhibits a well-defined nanorod morphology (Figure S20, Supporting Information). Cyclic voltammetry performed at a scan rate of 1 mV s^{-1} (Figure S21, Supporting Information) displays comparable redox peaks in both Zn/PAP/ZVO and Zn/PAM/ZVO full batteries, which are characteristic of reversible H^+/Zn^{2+} (de)intercalation. Notably, the PAP-based full battery demonstrates a markedly stronger current response, suggesting improved charge transfer kinetics, enhanced redox reversibility, and increased attainable capacity. Based on galvanostatic charge/discharge (GCD) measurements, a systematic comparison was performed to evaluate the specific capacity and rate capability of full batteries incorporating different hydrogel electrolytes, highlighting the structural advantages of the PAP system (Figure S22, Supporting Information). The Zn/PAP/ZVO battery exhibits outstanding energy storage performance, achieving specific capacities of 368.3, 356.7, 336.8, 306.5, 280.6, and 239.6 mAh g^{-1} at current densities of 0.2, 0.5, 1, 2, 3, and 5 A g^{-1}, respectively (**Figure 5a**). When the current density is returned to 0.2 A g^{-1}, the capacity recovers to 367.7 mAh g^{-1}, demonstrating excellent electrochemical reversibility. By comparison, the Zn/PAM/ZVO full battery delivers a significantly lower capacity of only 181.8 mAh g^{-1} at 5 A g^{-1}. This notable performance gap further confirms that the PHEA chain could enhance ion transport and reaction kinetics. Compared to the Zn/PAM/ZVO battery, the Zn/PAP/ZVO battery exhibits higher overall charge/discharge voltages. At a current density of 0.2 A g^{-1}, it shows a reduced voltage gap between the charge and discharge plateaus alongside an enhanced CE (Figure S23, Supporting Information). These observations indicate diminished polarization within the Zn/PAP/ZVO cell and the absence of rapid capacity decay in any specific voltage range. Furthermore, the Zn/PAP/ZVO battery exhibits a less distinct voltage plateau than the Zn/PAM/ZVO battery, which is attributable to its lower internal resistance and improved cathode/electrolyte interface chemistry. Long-term cycling tests further validate that the PAP-based battery maintains 87.2% of its initial capacity after 1000 cycles, significantly exceeding the 71.0% retention observed in the PAM-based system. Additionally, the cell demonstrates consistent CE close to 100% throughout the extended cycling test, as shown in Figure 5b. SEM characterization was conducted on the cycled ZVO cathode to explore its interfacial compatibility with the hydrogel electrolyte (Figure S24, Supporting Information). The maintained morphology of the ZVO cathode in the PAP system directly points to highly reversible Zn^{2+} insertion/extraction processes and effective inhibition of parasitic reactions. The remarkable electrochemical performance, including maximum specific capacity, rate capability, and cycling stability, enabled by the PAP hydrogel electrolyte, positions it competitively among contemporaneous research works (Table S4, Supporting Information).

To characterize the interfacial charge transfer properties, EIS was conducted on both battery configurations, and the resulting Nyquist plots were interpreted using equivalent circuit modeling. As illustrated in Figure S25 (Supporting Information), the PAP-based ZIB exhibits a significantly lower R_{ct} value of 142.5 Ω compared to the PAM-based system (237.9 Ω) at 25 °C. This result aligns well with the enhanced rate capability observed in the PAP system, which can be attributed to the rationally designed hydrogel electrolyte structure. In situ EIS of different hydrogel electrolytes was conducted to validate the improved charge transfer at the electrode/electrolyte interface (Figure 5c,d). The PAP-containing system shows lower, more stable values for both R_{ct} and diffusion resistance (R_{diff}) during cycling. This suggests that the introduction of PHEA efficiently regulates the interfacial environment by facilitating Zn^{2+} transport, thereby achieving highly stable charging/discharging processes. Interfacial stability was further assessed using a self-discharge test conducted over 48 h following full charging. As summarized in Figure 5e and Figure S26 (Supporting Information), the PAP-based battery retains 94.71% of its initial capacity, substantially higher than the 68.62% retention achieved by the PAM-based system. This result highlights the exceptional self-discharge resistance of the PAP electrolyte configuration. Leveraging the optimized hydrogen-bond network in the PAP hydrogel, the performance of Zn//ZVO full batteries was systematically evaluated under extreme temperature conditions. The battery retains 95.6% of its initial capacity after 400 cycles at 50 °C and 68.2% after 400 cycles at –20 °C (Figure 5f,g). These robust electrochemical behaviors position the PAP hydrogel as a highly suitable electrolyte for energy storage devices operating under demanding thermal environments. To elucidate the mechanism behind the superior cycling stability of the PAP hydrogel-based full battery at 50 °C and –20 °C, EIS tests were performed to probe ion transport dynamics (Figure S27, Supporting Information). The EIS results reveal that the PAP-based Zn//ZVO full battery maintains significantly lower interfacial resistances and more stable charge transfer processes compared to the counterpart, which effectively suppresses parasitic reactions and ensures highly reversible Zn plating/stripping. Furthermore, the minimal change in bulk resistance confirms excellent retention of ionic conductivity, even at –20 °C, thereby guaranteeing sufficient ion flux for battery operation under extreme temperatures.

As a proof of concept, functional pouch cells were fabricated using the PAP hydrogel electrolyte to demonstrate its technological viability (Figure 5h). The two serially connected pouch cells showed an initial open-circuit voltage of 3.16 V (Figure S28, Supporting Information), confirming proper assembly and an optimal initial electrochemical condition. Beyond laboratory characterization, the PAP-based Zn//ZVO pouch cell effectively powered an electric fan, underscoring its practical applicability.

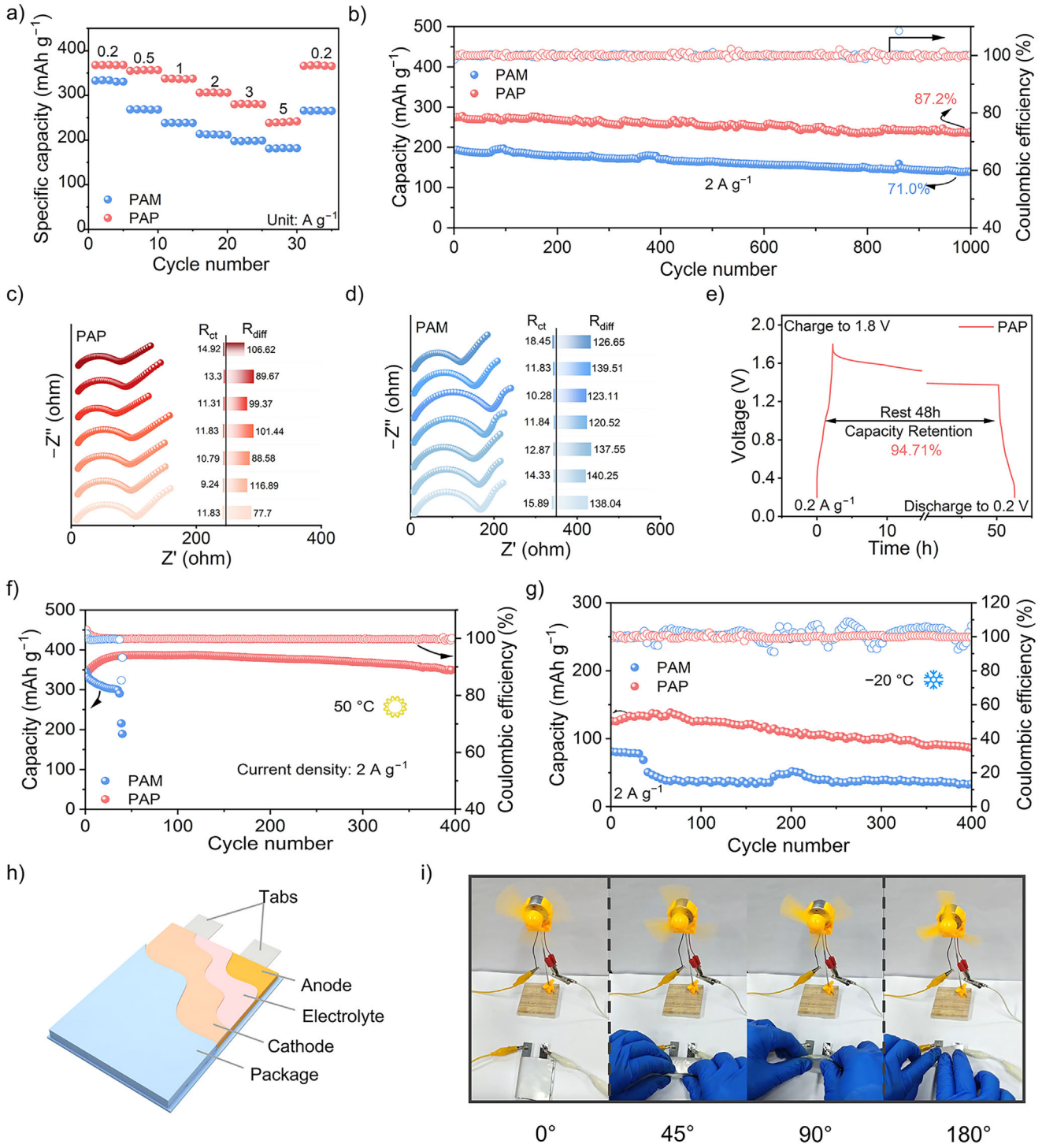

Figure 5. a) Rate performances of full batteries at 0.2 to 5 A g^{-1}. b) Cycling performances at 2 A g^{-1}. In situ EIS spectra of full batteries using c) PAP and d) PAM hydrogel electrolytes. e) Self-discharge curves of Zn/PAP/ZVO. Cycling performances at f) 50 °C and g) –20 °C. h) The assembled diagram of the pouch cell. i) The displays of the pouch cell under different bending states.

Flexibility is a critical requirement for pouch cells, yet mechanical stress from bending or extrusion can cause active material detachment, interface degradation, and structural failure, leading to irreversible performance loss. As demonstrated in Figure S29 (Supporting Information), a pouch cell incorporating the PAP hydrogel overcomes this challenge, retaining 91.7% of its capacity even after severe 180° folding and thereby highlighting exceptional mechanical-electrochemical integrity. The cell remained fully functional after undergoing 180° mechanical folding (Figure 5i), which is essential for commercial wearable energy storage devices.

3. Conclusion

In summary, we developed a multifunctional hydrogel electrolyte by copolymerizing AM with PHEA. The molecular structure of PHEA introduces beneficial non-covalent interactions that significantly enhance the stability of the Zn anode and the battery's temperature adaptability. The aromatic groups establish π-anion interactions that confine OTf^- anions while promoting rapid Zn^{2+} transport. Simultaneously, the oxygen-rich motifs synergize with AM's amide groups to restrict water activity, thereby inhibiting the HER, accelerating Zn^{2+} desolvation, and improving thermal resilience. Consequently, the Zn//Zn symmetric cell using the PAP electrolyte exhibits exceptional cycling stability, operating for over 6400 h at 25 °C, 2400 h at 50 °C, and 1200 h at –20 °C (1 mA cm^{-2}/1 mAh cm^{-2}). When configured in a Zn//ZVO full battery, the system achieves a capacity retention of 87.2% after 1000 cycles at 2 A g^{-1} under ambient conditions, along with remarkable cycling performance at both elevated and subzero temperatures. These findings provide valuable insights for designing advanced hydrogel electrolytes and pave the way for developing long-lasting, practical ZIBs.

Supporting Information

Supporting Information is available from the Wiley Online Library or from the author.

Acknowledgements

The authors appreciate the financial support by the National Natural Science Foundation of China (22272150 and 22502176), the Zhejiang Provincial Natural Science of China (LZ23B030001), and the Major Science and Technology Project of Jinhua City (2023-1-060). The calculations were carried out on high performance supercomputer of Zhejiang Normal University.

Conflict of Interest

The authors declare no conflict of interest.

Data Availability Statement

Research data are not shared.

Keywords

π-anion interaction, hydrogel electrolyte, hydrogen bond reconstruction, wide temperature adaptation, Zn anode

Received: October 20, 2025
Revised: November 17, 2025
Published online: November 29, 2025

[1] C. Guo, J. Zhou, Y. Chen, H. Zhuang, J. Li, J. Huang, Y. Zhang, Y. Chen, S. L. Li, Y. Q. Lan, *Angew. Chem., Int. Ed.* **2023**, *62*, 202300125.
[2] Z. Shen, Y. Liu, Z. Li, Z. Tang, J. Pu, L. Luo, Y. Ji, J. Xie, Z. Shu, Y. Yao, N. Zhang, G. Hong, *Adv. Funct. Mater.* **2024**, *35*, 2406620.
[3] Y. Chen, B. Yin, Y. Zeng, H. Wang, B.-B. Xie, D. Luan, Y. Hu, X. W. Lou, *Chem* **2025**, *11*, 102411.
[4] F. Yang, C. Tian, L. Bai, T. Zhang, H. Wang, J. Ning, Y. Hu, *Compos. Part B-Eng.* **2025**, *301*, 112528.
[5] Y. Liu, L. Miao, H. Shen, Z. Wang, K. Yao, Y. Hu, J. Sun, S. Hou, J. Zhao, K. Yang, *Adv. Funct. Mater.* **2025**, *35*, 2501968.
[6] K. Wang, H. Zhan, X. X. Liu, X. Sun, *Adv. Funct. Mater.* **2024**, *35*, 202418993.
[7] X. Xiao, X. Ye, Z. Wu, X. Wu, J. Yu, L. Gu, S. Liu, *Adv. Mater.* **2024**, *36*, 2408706.
[8] H. Lu, B. Yin, T. Zhang, Y. Shao, J. Zhong, H. Wang, B.-B. Xie, Y. Zhong, Y. Hu, *ACS Appl. Mater. Interfaces* **2025**, *17*, 21234.
[9] R. Gao, J. Wang, Y. Song, K. Li, Z. Chen, Q. Shen, Y. Wang, *Adv. Funct. Mater.* **2025**, *36*, 14585.
[10] X. Yang, J. Zhou, B. Hao, B. Shen, Q. Qian, Z. Wang, C. Yan, T. Qian, *Adv. Mater.* **2025**, *37*, 2506537.
[11] Q. Nian, T. Sun, Y. Li, S. Jin, S. Liu, X. Luo, Z. Wang, B. Q. Xiong, Z. Cui, D. Ruan, H. Ji, Z. Tao, X. Ren, *Angew. Chem., Int. Ed.* **2023**, *62*, 202217671.
[12] M. Chen, W. Zhou, A. Wang, A. Huang, J. Chen, J. Xu, C.-P. Wong, *J. Mater. Chem. A* **2020**, *8*, 6828.
[13] Z. Yan, F. Luo, S. Yang, Q. Wu, J. Zhang, X. Liu, J. Huang, Y. Chen, *Adv. Funct. Mater.* **2025**, *37*, 14679.
[14] J. Liu, J. Long, Z. Shen, X. Jin, T. Han, T. Si, H. Zhang, *Adv. Sci.* **2021**, *8*, 2004689.
[15] X. Wang, P. Lei, C. Zheng, Z. Wang, B. Wang, X. Cui, J. Cheng, *Adv. Funct. Mater.* **2025**, *35*, 2500916.
[16] Q. Wu, J. Zhang, S. Yang, F. Luo, Z. Yan, X. Liu, H. Xie, J. Huang, Y. Chen, *Angew. Chem., Int. Ed.* **2025**, *64*, 202418524.
[17] H. Lu, J. Hu, L. Wang, J. Li, X. Ma, Z. Zhu, H. Li, Y. Zhao, Y. Li, J. Zhao, B. Xu, *Adv. Funct. Mater.* **2022**, *32*, 2112540.
[18] S. Yang, Q. Wu, Y. Li, F. Luo, J. Zhang, K. Chen, Y. You, J. Huang, H. Xie, Y. Chen, *Angew. Chem., Int. Ed.* **2024**, *63*, 202409160.
[19] Z. J. Chen, T. Y. Shen, X. Xiao, X. C. He, Y. L. Luo, Z. Jin, C. H. Li, *Adv. Mater.* **2024**, *36*, 2413268.
[20] W. Zhang, F. Guo, H. Mi, Z.-S. Wu, C. Ji, C. Yang, J. Qiu, *Adv. Energy Mater.* **2022**, *12*, 2202219.
[21] J. Li, H. Zhang, Z. Liu, H. Du, H. Wan, X. Li, J. Yang, C. Yan, *Adv. Funct. Mater.* **2024**, *35*, 2412865.
[22] Y. Lei, F. Liu, L. Chen, M. Xu, Y. Hu, T. Abdiryim, F. Xu, J. You, Y. Tan, Z. Tan, X. Liu, *Nano Energy* **2025**, *143*, 111284.
[23] H. Xia, G. Xu, X. Cao, C. Miao, H. Zhang, P. Chen, Y. Zhou, W. Zhang, Z. Sun, *Adv. Mater.* **2023**, *35*, 2301996.
[24] H. Yorita, K. Otomo, H. Hiramatsu, A. Toyama, T. Miura, H. Takeuchi, *J. Am. Chem. Soc.* **2008**, *130*, 15266.
[25] Q. Wu, J. Huang, J. Zhang, S. Yang, Y. Li, F. Luo, Y. You, Y. Li, H. Xie, Y. Chen, *Angew. Chem., Int. Ed.* **2024**, *63*, 202319051.
[26] C. L. Xie, S. F. Liu, H. Wu, Q. Zhang, C. Hu, Z. F. Yang, H. H. Li, Y. G. Tang, H. Y. Wang, *Sci. Bull.* **2023**, *68*, 1531.
[27] F. Luo, S. Yang, Q. Wu, Y. Li, J. Zhang, Y. Zhang, J. Huang, H. Xie, Y. Chen, *Energy Environ. Sci.* **2024**, *17*, 8570.
[28] S. Yamada, *Chem. Rev.* **2018**, *118*, 11353.
[29] Z. Zhang, X. Lan, G. Liao, W. Du, Y. Zhang, M. Ye, Z. Wen, Y. Tang, X. Liu, C. C. Li, *Angew. Chem., Int. Ed.* **2025**, *64*, 202503396.

[30] Y. Wang, Q. Li, H. Hong, S. Yang, R. Zhang, X. Wang, X. Jin, B. Xiong, S. Bai, C. Zhi, *Nat. Commun.* **2023**, *14*, 3890.
[31] G. Zhao, A. Zhang, X. Chen, G. Xiang, T. Jiang, X. Zhao, *Bioact. Mater.* **2024**, *41*, 46.
[32] X. Lin, X. Wang, L. Zeng, Z. L. Wu, H. Guo, D. Hourdet, *Chem. Mater.* **2021**, *33*, 7633.
[33] G. Zhang, W. Fu, J. Zhu, Z. Xue, T. Qiu, P. Lu, X. Yu, X.-X. Liu, X. Sun, *Adv. Funct. Mater.* **2025**, *35*, 11607.
[34] K. Wang, Y. Luo, H. Zhan, X.-X. Liu, X. Sun, *ACS Nano* **2024**, *18*, 27672.
[35] R. Han, T. Jiang, Z. Wang, R. Xue, X. Liu, Y. Tang, Z. Qi, Y. Ma, *Adv. Funct. Mater.* **2025**, *35*, 2412255.
[36] R. Liang, H. Yu, L. Wang, L. Lin, N. Wang, K.-u.-R. Naveed, *ACS Appl. Mater. Interfaces* **2019**, *11*, 43563.
[37] L. Ma, T. P. Pollard, Y. Zhang, M. A. Schroeder, M. S. Ding, A. V. Cresce, R. Sun, D. R. Baker, B. A. Helms, E. J. Maginn, C. Wang, O. Borodin, K. Xu, *Angew. Chem., Int. Ed.* **2021**, *60*, 12438.
[38] G. Ma, L. Miao, Y. Dong, W. Yuan, X. Nie, S. Di, Y. Wang, L. Wang, N. Zhang, *Energy Storage Mater.* **2022**, *47*, 203.
[39] X. Liang, X. Chen, Z. Zhai, T. Yu, H. Yu, H. Wang, D. Meng, L. Peng, S. Yin, *Chem. Eng. J.* **2024**, *493*, 152622.
[40] H. Wang, W. Ye, B. Yin, K. Wang, M. S. Riaz, B.-B. Xie, Y. Zhong, Y. Hu, *Angew. Chem., Int. Ed.* **2023**, *62*, 202218872.
[41] S.-J. Guo, M.-Y. Yan, D.-M. Xu, P. He, K.-J. Yan, J.-X. Zhu, Y.-K. Yu, Z.-Y. Peng, Y.-Z. Luo, F.-F. Cao, *Energy Environ. Sci.* **2025**, *18*, 418.
[42] S. Ma, J. Zhao, H. Xiao, Q. Gao, F. Li, C. Song, G. Li, *Angew. Chem., Int. Ed.* **2024**, *64*, 202412955.
[43] J. Ba, X. Yin, F. Duan, Y. Cheng, X. Pu, Y. L. Zhu, Y. Wei, Y. Wang, *Small Methods* **2024**, *8*, 202301731.
[44] T. Zhou, J. Wang, L. Lv, R. Li, L. Chen, S. Zhang, H. Zhang, B. Ma, J. Huang, B. Wu, L. Chen, T. Deng, X. Fan, *Energy Environ. Sci.* **2024**, *17*, 9185.
[45] Y. He, R. Zhang, P. Zou, R. W. Chu, R. Lin, K. Xu, H. L. Xin, *J. Am. Chem. Soc.* **2025**, *147*, 6427.
[46] F. Zhang, M. Yang, P. Fang, J. Yu, X. Ma, Y. Hu, F. Yan, *J. Mater. Chem. A* **2024**, *12*, 3470.
[47] S. Li, Y. Zhong, J. Huang, G. Lai, L. Li, L. Jiang, X. Xu, B. Lu, Y. Liu, J. Zhou, *Energy Environ. Sci.* **2025**, *18*, 2599.
[48] G. Guo, C. Ji, J. Lin, T. Wu, Y. Luo, C. Sun, M. Li, H. Mi, L. Sun, H. J. Seifert, *Angew. Chem., Int. Ed.* **2024**, *63*, 202407417.
[49] R. Huang, J. Zhang, W. Wang, X. Wu, X. Liao, T. Lu, Y. Li, J. Chen, S. Chen, Y. Qiao, Q. Zhao, H. Wang, *Energy Environ. Sci.* **2024**, *17*, 3179.
[50] R. Sun, D. Han, C. Cui, Z. Han, X. Guo, B. Zhang, Y. Guo, Y. Liu, Z. Weng, Q.-H. Yang, *Angew. Chem., Int. Ed.* **2023**, *62*, 202303557.